Synthesis and physico-chemical characteristics of nanosized particles produced by laser ablation of a nickel target in water

R. Mahfouz, F.J. Cadete Santos Aires, A. Brenier, B. Jacquier, J.C. Bertolini

Synthesis and physico-chemical characteristics of nanosized particles produced by laser ablation of a nickel target in water

R. Mahfouz [a], F.J. Cadete Santos Aires [a,*], A. Brenier [b], B. Jacquier [b], J.C. Bertolini [a]

[a] *IRCELYON, Institut de Recherches sur la Catalyse et l'Environnement de Lyon, UMR 5256, CNRS - Université Claude Bernard Lyon I, 2 Avenue Albert Einstein, 69626 Villeurbanne Cedex, France*

[b] *LPCML, Laboratoire de Physico-Chimie des Matériaux Luminescents, UMR 5620, CNRS - Université Claude Bernard Lyon I, 10 Rue A.M. Ampère, 69622 Villeurbanne Cedex, France*

Ablation of Ni targets in water by laser impact (532 nm, 40 mJ/pulse, 10 Hz and 8 ns duration) focused on massive samples (∼2 mm diameter) generates colloids with fine nanoparticles. The amount of metal released in the solution (measured by mass loss of the target or ICP) was found to increase first linearly with time, but slower after 8 min of impact. The size distribution of the nanoparticles thus produced was measured (by TEM) to be in the range 3–5.3 nm in diameter, with a tendency for the size to be smaller for larger number of laser shots. Actually, nickel oxide nanoparticles were produced, rather than nickel nanoparticles as it was shown by HRTEM. XPS photoemission measurements evidenced the presence of nickel oxide species on the crater of the nickel sample surface after laser ablation.

Keywords: Ni; NiO; Nanoparticles; Laser ablation in liquid phase; HRTEM; XPS photoemission

1. Introduction

In recent years, many researches have been done on noble metal nanoparticles because of their unique character differing from those in bulk state. Metal colloids are one of the important nanosize materials that will open significant opportunities in chemistry and material science [1]. Metal colloid nanoparticles have a great interest because of the size dependence of their optical properties, magnetic properties, catalytic activities, etc. [2,3]. Indeed, metal nanoparticles have magnetic properties different of bulk materials of the same composition due to the coupling of magnetism with structure, surface effects, and thermally activated processes [4,5]. Gold nanoparticles smaller than 5 nm in diameter have an intense photoluminescence [6] and those with a diameter smaller than 10 nm show significant catalytic activities in low temperature CO oxidation [3,6,7]. Besides, laser ablated suspended metal nanoparticles prepared in liquid phase can be used directly for catalysis purposes. For instance, it was shown that (bare or stabilized by a surfactant) palladium nanoparticles can be efficient for several target hydrogenation reactions [8] and that nickel particles exhibit a catalytic effect for the preparation of 3-aryl propanenitrile from benzylchloride and bromoacetonitrile under mild conditions without any activation, whereas Ni particles larger than submicrometer size have not shown this activity [9].

Thus, metal nanoparticles may have specific physical and chemical properties depending upon their size and/or morphology. It exists many ways to produce nanoparticles. Among them, ablation of metals by laser vaporization from a bulk target in liquid environment is a rather simple method which has attracted recently some attention [8–20]. But, the characteristics of the metal particles formed and the ablation efficiency strongly depend upon many parameters such as the wavelength of the laser impinging the metallic target [10,13,16], the duration of the laser pulses (in the femto-, pico- and nanosecond regime) both in liquid and gas phase [11,21], the laser fluence [10,16,18,19], the ablation time duration [16] and the effective liquid medium, with or without the presence of surfactants [19]. The laser fluence is one of the most important parameters. Indeed, the ejection of metal particles from the target requires a minimum power (or fluence) [11,19]. The mean size of the

* Corresponding author. Tel.: +33 472445303; fax: +33 472445399.
E-mail address: francisco.aires@irecelyon.univ-lyon1.fr
(F.J. Cadete Santos Aires).

nanoparticles has been found generally to increase with increasing laser fluence and is generally smallest for fluences not too far above the laser breakdown threshold [10]. But, for platinum it has been shown that at low laser fluence compounds with platinum in a non-zero oxidation state can be produced, probably due to the presence of a large percentage of metal atoms, together with small clusters, which could be able to react with the liquid medium [18]. Besides the laser fluence, the number of laser shots (i.e. the time spent during laser vaporization) must influence the concentration and the morphology of metal particles released in a liquid. For longer times under the laser beam the metal particle concentration is expected to increase, but it can saturate due to light absorption in the colloid highly concentrated in metal particles [19]. Moreover, nanoparticles can be modified in size and shape due to their further interaction with the laser light passing through [13,22]. But, the interaction between a laser pulse and a solid target in a confining liquid is not obvious and its mechanism is not well understood (see for instance the review of paper of Yang [23]). In any case, it is a way to synthesize nanocrystals and nanostructures ([23] and references therein).

In the present study, suspensions of nanoparticles were prepared by laser ablation in water from a pure nickel target, at various laser interaction times (number of laser shots). Morphology and structure of the nanoparticles obtained in the colloidal solutions were characterized mainly by transmission electron microscopy (TEM and HRTEM). Measurements of the weight loss of the target after laser ablation and chemical analysis (ICP) were used to determine the amount of metal released in the aqueous solution. In addition, UV–vis spectrometry was tentatively employed to characterize further the properties of the particles in suspension. XPS photoelectron spectra of the impacted region of the sample were also measured in order to gain complementary information.

2. Experimental

The laser ablation method was employed to fabricate particle suspensions.

The nickel samples used as metal sources were in shape of discs of about 10 mm diameter and 1.5 mm thickness. They were obtained by cutting a high purity (>99.95%) nickel single crystal bar by spark erosion; they are further mechanically polished (down to 1 μm) and cleaned by ultrasonication into dried acetone and then ethanol in sequence, before use as metallic sources. The Ni sample was fixed onto a Teflon support plugged onto a glass vessel containing approximately 5 cm^3 of distilled water and closed by a welded glass (or quartz) window (Fig. 1). The nickel target is completely immersed which secures a liquid/solid interface free of gas. A Nd:YAG laser operating at the second harmonic ($\lambda = 532$ nm, pulse duration = 8 ns, 10 Hz) was focused (∼2 mm in diameter) on the target. The laser power was fixed at 40 mJ/pulse. The ablation time was varied from 2 to 15 min.

The amount released in the aqueous solution by the laser ablation was measured from the weight loss of the metal plate after the laser ablation. The precision of the (Sartorius) balance was ±1 μg.

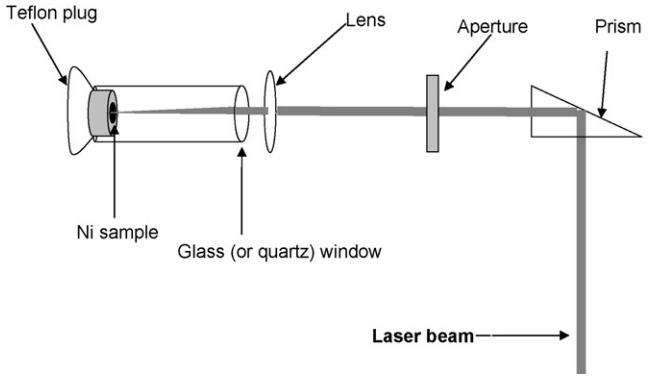

Fig. 1. Experimental setup for laser ablation.

Induced coupled plasma (ICP) chemical analysis was used to determine the metal contents. The colloidal solutions of nanoparticles were evaporated in a quartz container, and then the nickel nanoparticles were dissolved in an acid solution ($H_2SO_4 + HNO_3$). The solutions were filtered before analysis by optical ICP in a SPECTRO monochromatic spectrophotometer (Ni wavelength: 231,604 nm).

The optical absorption spectra of colloids were measured by UV–vis spectrometry with using a Perkin-Elmer Lambda 35 spectrometer working in the 190–1000 nm range and equipped with a photodiode detector. Standard quartz optical cells of QS-type (with 10 mm light path) were employed; the scanning velocity used was 120 nm/min with an interval of 2 nm.

The morphology and structure of the particles obtained by laser ablation in water were studied by transmission electron microscopy (TEM). We used a JEOL JEM 2010 microscope operated at 200 kV, equipped with a LaB_6 tip, a high resolution pole-piece (0.196 nm point resolution and 0.14 nm limit information) and a Pentafet-LinK ISIS energy dispersive X-ray (EDX) spectrometer (Oxford Instruments). The samples were prepared by simply putting a drop of the solution containing the particles on a holey-carbon thin film supported on a microscopy copper grid (3.05 mm, 200 mesh).

The particle size was determined from the size histograms (performed over more than 400 particles) measured from TEM images. High-resolution imaging gave insight on the structure of the nanoparticles and allowed the determination of the structural phases and local orientations. Interplanar distances (d) and angles (α) were measured either directly on the HRTEM images or by performing 2D-FFTs on the resolved regions and/or particles on those images. Since the regions and/or nanoparticles used to perform 2D-FFT are quite small (a few nm), only very few interplanar distances contribute to the measurement yielding small variations on the measured interplanar distances and angles: typically ±0.01 nm for d and ±1° for α.

EDX analysis was performed in order to check the presence (or not) of impurities.

XPS experiments were carried out in a KRATOS AXIS Ultra DLD spectrometer using a hemispherical analyzer and working

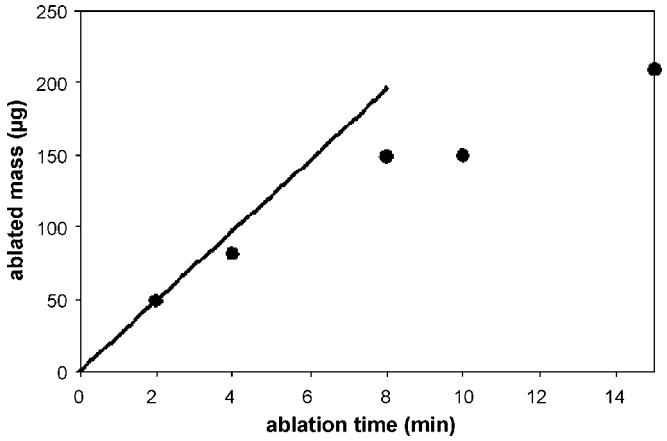

Fig. 2. Mass of nickel (μg) released in pure water measured as a function of time of ablation (min), the black line shows the linear estimated evolution of nickel concentration in pure water as a function of time (see text for further details).

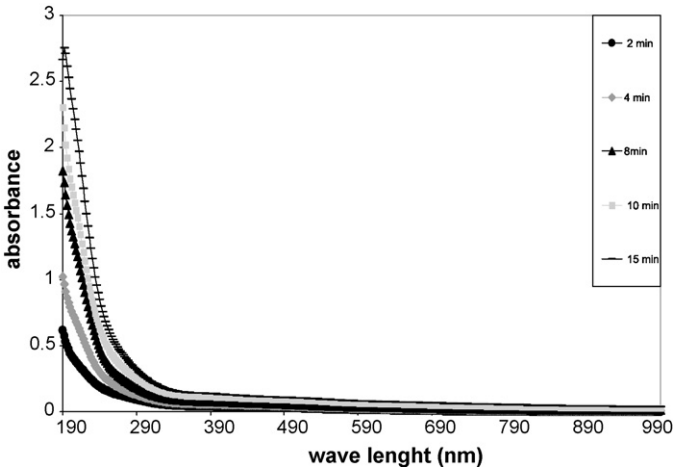

Fig. 3. UV–vis absorption spectra of Ni colloids obtained in water for 2, 4, 8, 10 and 15 min of laser ablation.

at a vacuum better than 10^{-9} mbar. All the data were acquired using a monochromatic Al Kα X-ray source (1486.6 eV, 150 W), pass energy of 20 eV and a hybrid lens mode. Measurements were performed on different regions of the sample surface, with an analyzed area fixed at 700 μm × 300 μm. In addition, 4 keV Ar^+ ion bombardment was used to clean the Ni surface in order to obtain a reference spectrum for clean nickel. Quantitative analysis were performed on the basis of Ni $2p_{3/2}$ and O 1s characteristic spectra, after subtraction of a Shirley-type background.

3. Results and discussion

The weight loss of the metal plate after the laser ablation versus time is shown in Fig. 2 and Table 1. The black line in Fig. 2 characterizes the mass expected for a process where the ablation efficiency is constant in time. The mass of the nickel nanoparticles increases as time of ablation increases (Fig. 2) but the efficiency of ablation decreases with time of ablation since the mass of ablated nickel increases slower than expected (black line in Fig. 2). Such effect was also observed by Mafuné et al. for Pt in water [19]. This can be related either to the abundance of the nanoparticles in liquid which could interact with the laser beam and thus could lower the laser power on the metal plate or to the modification of the surface properties of the metal plate by the irradiation of the pulsed laser which could diminish the ablation efficiency.

The amount of nickel deduced from ICP show the same tendency as the weight loss of the target measured by the Sartorius balance, but the values are not strictly proportional (Table 1). This can be due to some difficulties to collect properly the whole metal in the solution or/and to an incomplete dissolution of the metal in the acid solution before ICP analysis.

Optical absorption spectra of nickel nanoparticles in water exhibit structureless broad bands whose intensity decreases continuously above 190 nm (Fig. 3). Therefore, one cannot get information about the size/morphology of the metal particles. Nevertheless, one sees that the UV light absorption increases with the metal abundance in the solution.

3.1. Morphologic and structural characterization

The particles synthesized by laser ablation in solution were characterized by transmission electron microscopy in order to determine their size distribution, morphology and structure (HRTEM). EDX local analysis (by varying the size of the electron probe) showed that there are no impurities associated with particles. The quantification of oxygen within the nanoparticles is not very precise since there is always some inhomogeneously spread oxygen associated with the amorphous carbon of the supporting film and so we could not determine the stoichiometry of the particles by this method.

Fig. 4 shows the particles obtained for different times of ablation with the corresponding size distributions. The mean diameters and the standard deviations are summarised in Table 1. Nickel nanoparticles having a mean diameter in the range 3–5.3 nm are actually obtained. One can see that the mean size and the percentage of large particles decrease with

Table 1
Characteristics of the Ni nanoparticles

Sample Ni (ablation time in min)	Weight (μg)	ICP (μg)	Mean diameter (nm)	Standard deviation
2	49	34	5.3	±4.2
4	82	71	3.6	±2.4
8	149	87	3.7	±1.5
10	150	96.5	3.4	±1.7
15	210	154	3	±1.6

ablation time. This can be explained by a redistribution of the size of the particles through their interaction with the laser beam.

We can distinguish two types of particles:

(i) The smaller ones (up to around 8 nm) are single crystalline, mostly pseudo-round-shaped and some times pseudo-parallelipipedic-shaped (Figs. 5 and 6).

(ii) The larger ones are either polycrystalline, containing internal structural defects or exhibiting core–shell contrast with typical Moiré patterns (Fig. 7).

The former sort of particles always exhibit interplanar distances and angles typical of fcc NiO ($a = b = c = 0.4177$ nm). This is true even for the smaller particles as the one represented in Fig. 5 which is only 1.3 nm. Basically we observe two different

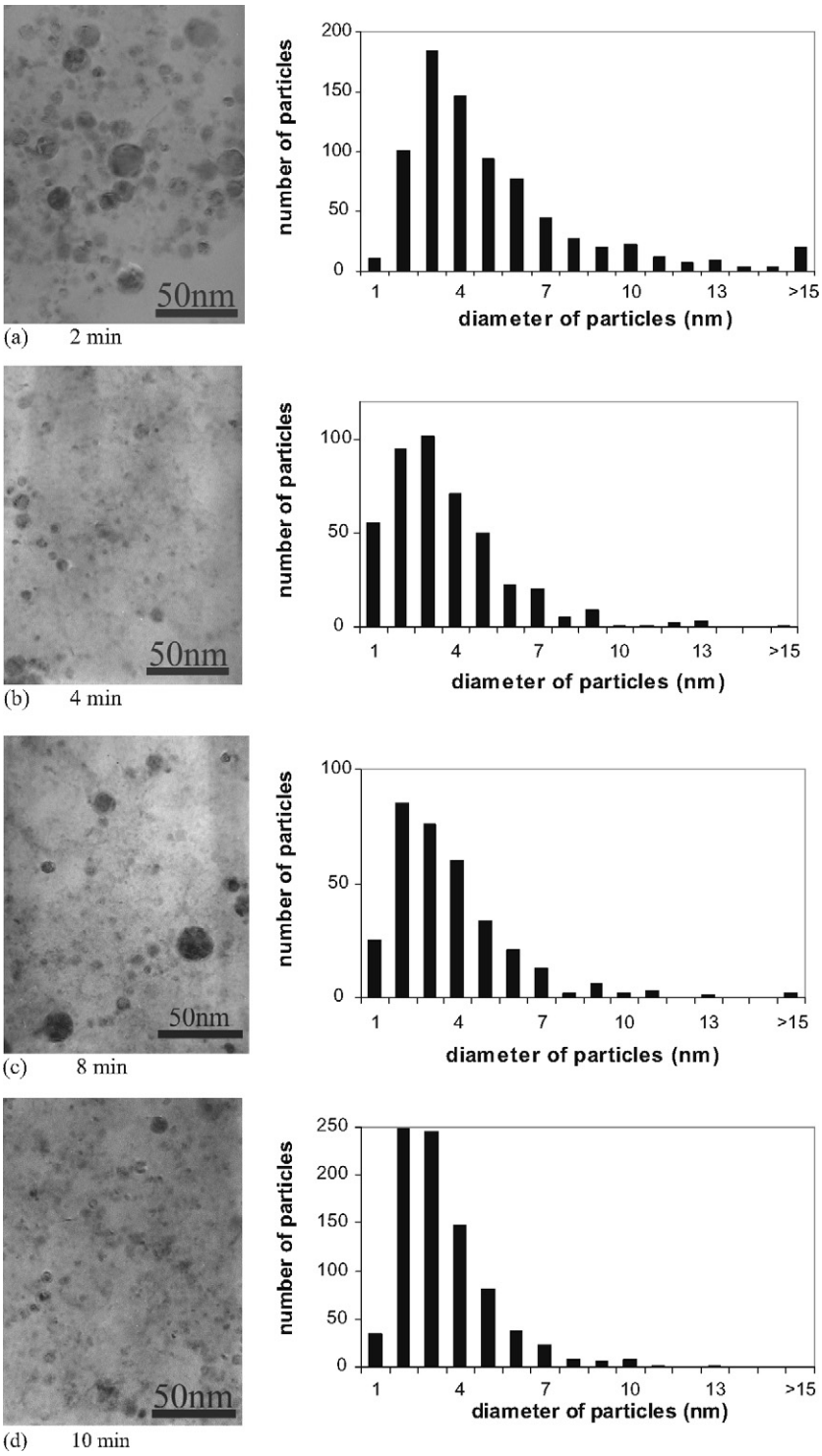

Fig. 4. TEM images and size histograms for nickel nanoparticles obtained after 2 min (a), 4 min (b), 8 min (c), 10 min (d) and 15 min (e) of laser ablation.

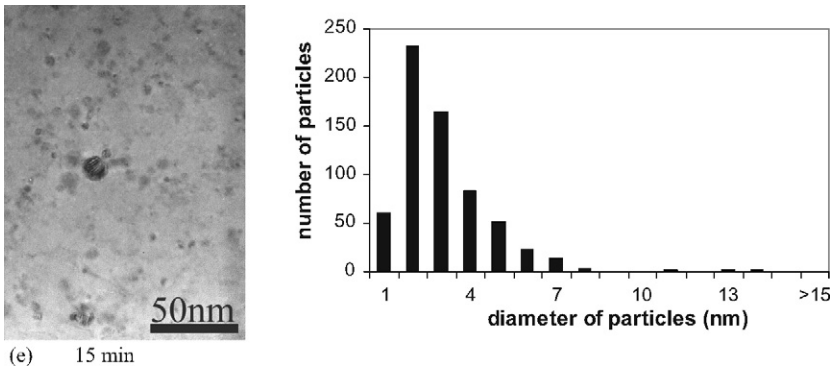

Fig. 4. (*Continued*).

types of orientation of the particles as it can be seen in Fig. 6. The observed interplanar distances correspond to type NiO (1 1 1) planes [$d_{(1\ 1\ 1)} = 0.241$ nm] and type NiO (1 0 0) planes [$d_{(2\ 0\ 0)} = 0.209$ nm; since there is an extinction for $d_{(1\ 0\ 0)}$ in fcc structured materials]. Thus the resolved orientations for the particles are of [0 0 1] (Fig. 6b, d and g) and [−1, 1, 0] (Fig. 6e) types. We can indeed identify type (1 0 0) distances with 90° angles between them in the former orientation whereas we identify type (1 1 1) and type (1 0 0) plane which exhibit 70.5° angles (between two (1 1 1) type planes) and 54.7° (between (1 1 1) and (1 0 0) type planes).

The latter type of particles (>8 nm) are very interesting especially since they can give us some hints on the formation of our nanoparticles. This is particularly the case of those that exhibit core–shell contrasts with Moiré patterns. The Moiré patterns arise from the interference of two different lattices and may be due to the presence of two crystalline phases surrounding or superposing each other. Indeed, in our case, we could determine that these particles are formed by a Ni central core surrounded by a NiO shell.

In Fig. 8, a nanoparticle (9 nm) exhibits an asymmetric core–shell structure as it is evidenced by the presence of the off-centred Moiré pattern on its right side (the NiO shell is much larger on the left side). The 2D-FFT of the shell (Fig. 8b) shows the presence of two interplanar distances S1 (0.241 nm) and S2 (0.209 nm) separated by an angle of 54.7° corresponding respectively to $d_{(1\ 1\ 1)}$ and $d_{(2\ 0\ 0)}$ in NiO. The 2D-FFT of the region with the Moiré pattern (Fig. 8c) shows the presence of six main spots S1, S2, C1, C2, M1 and M2. S1 and S2 correspond to the previously referred spots in Fig. 8b and can thus be attributed to the shell. A new set of values, C1 (0.203 nm) and C2 (0.176 nm) separated also by an angle of 54.7°, can be attributed to Ni which has also an fcc structure ($a = b = c = 0.3524$ nm). C1 and C2, respectively correspond thus to $d_{(1\ 1\ 1)}$ and $d_{(2\ 0\ 0)}$ in Ni. Furthermore C1 is perfectly aligned with S1 and C2 with S2 giving rise to two parallel Moiré spots M1 (1.30 nm) and M2 (1.15 nm), respectively. The relation between the Moiré pattern distance and the two different lattice distance at its origin is given by $D = d_1 d_2 / |d_1 - d_2|$ [24] which in our case gives the relations M1 = C1S1/|C1 − S1| = 1.29 nm and M2 = C2S2/|C2 − S2| = 1.12 nm. These values are very close to the measured ones and the low discrepancy is acceptable due to the poor precision of the measurement of large distances (corresponding to short distances – close to the central spot – in reciprocal space) in the 2D-FFT.

A peculiar example is the one treated in Fig. 9 where the surrounding NiO shell is uncomplete and there is still a Ni region of the particle at the periphery (Fig. 9b). Furthermore, the shell is polycrystalline with different regions with similar orientation but rotated with respect to each other (Fig. 9c–e). The Moiré region corresponding to where a NiO shell surrounds a Ni core presents similar characteristics to the previous example. In this case, two sets of spots can be attributed to $d_{(1\ 1\ 1)}$ type distances in NiO shell (S1: 0.241 nm; S1′: 0.241 nm) which are aligned with $d_{(1\ 1\ 1)}$ distances in Ni core (C1: 0.203 nm; C1′: 0.203 nm); the third set of distances is attributed to $d_{(2\ 0\ 0)}$ type distance in NiO shell (S2: 0.209 nm) aligned with $d_{(2\ 0\ 0)}$ type distance in Ni core (C2: 0.176 nm). This should give rise to the observation of three parallel Moirés; however only two are observed in the 2D-FFT (Fig. 9f). M1′ is not observed certainly due to the low periodicity in the corresponding direction that will give a very low signal in the FFT; however one can see three distances in the Moiré pattern in the micrograph of Fig. 9a. The two other Moiré distances corresponding to M1 (1.38 nm) and M2 (1.14 nm) are detected and, as for the previous example, correspond well to the expected ones within the measurement error.

Such core–shell effects were also observed by Liu et al. [25] during laser ablation of Ni targets in the presence of a partial pressure (40 Pa) of oxygen under vacuum conditions. In this case the core–shell structure seems to be related to a surface oxidation of the synthesized particles due to the presence of oxygen.

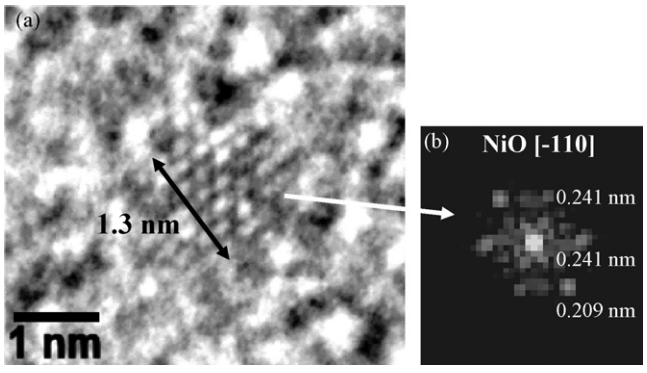

Fig. 5. HRTEM of a 1.3 nm NiO particle and corresponding 2D-FFT.

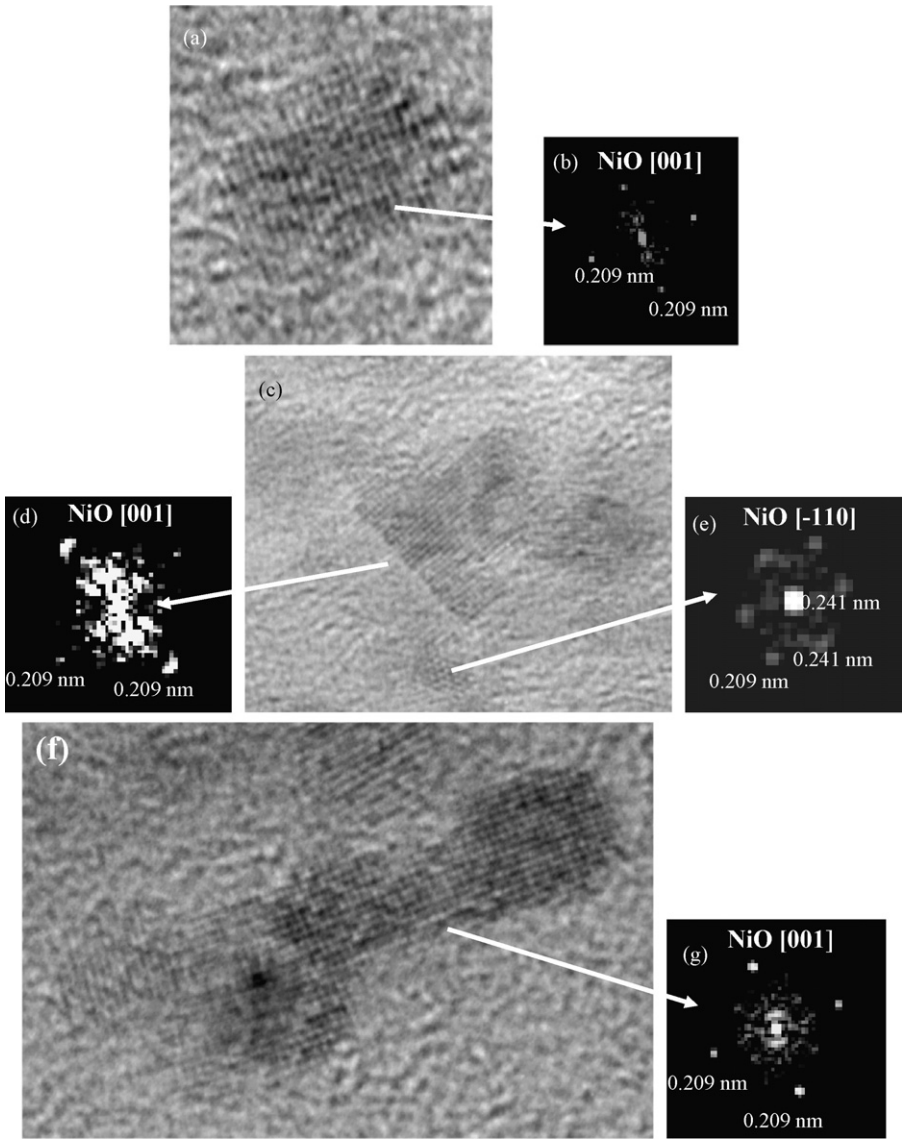

Fig. 6. HRTEM images (a, c and f) and corresponding 2D-FFTs (b, d, e, and g) showing that the particles formed have the cfc structure of NiO (see text for details).

Our observations lead us to think that the early stages of particle formation yield small nickel metal particles that can grow by accretion of several of those particles. These larger particles can undergo surface oxidation, due to partial decomposition of water under laser interaction, yielding the core–shell morphology and the polycrystalline particles that we observe. Smaller particles (<8 nm) are mainly single crystalline NiO. This can either be attributed to total oxidation of the Ni particles formed in the early stages or to laser ablation of an oxidised or hydroxilated Ni target during laser interaction process. A surface analysis study of the target surface before and after ablation presented hereafter shows that this latter possibility is confirmed.

3.2. Surface analysis of the target surface

It is a priori surprising that laser ablation from a pure Ni target yield NiO nanoparticles. But, this can be the consequence of chemical reactions which could take place at the interface between the liquid (water) and the laser induced plasma (containing Ni atoms and ions) due to the high temperature and high pressure in front of the laser induced plasma [23]. However, one can also suppose that some oxidation of the surface of the Ni target could occur during the laser ablation process. For this purpose, XPS photoemission measurements were performed on various regions of the target after laser production of the nanoparticles: (i) the zone impacted (10 min) by the laser beam, (ii) one region out of the laser impact zone and (iii) clean Ni obtained by Ar^+ ion bombardment of the ''out of the laser impact zone'' region directly in the XPS spectrometer. XPS measurements were made on two different areas for each zone leading to quite similar results.

The XPS spectra for the Ni 2p and O 1s regions are reported in Figs. 10 and 11. In order to obtain complementary information on the chemical state of the species present at

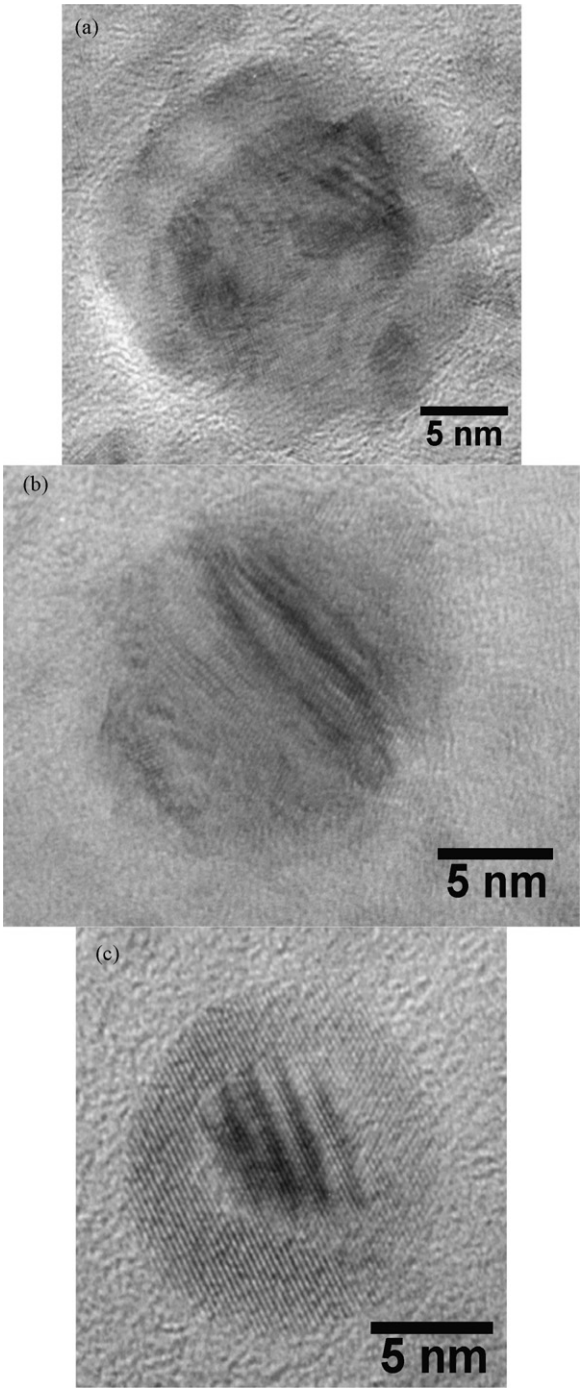

Fig. 7. HRTEM images of large particles: (a) polycrystalline particle, (b) particle with multiple defects and (c) core–shell particle exhibiting a central Moiré.

the surface of the samples, characteristic LMM Auger peaks of Ni are also reported as complement of the XPS peaks (Fig. 12).

After laser ablation, the spectra obtained both for the ''laser impact zone'' and ''out of the laser impact zone'' show additional structures in the Ni $2p_{3/2}$ region with respect to clean Ni (Fig. 10); one can clearly see additional peaks located nearby 854 and 856 eV. They are very probably due to nickel oxides. This is coherent with the observation of a loss peak at ~861 eV which is actually present on various nickel oxides

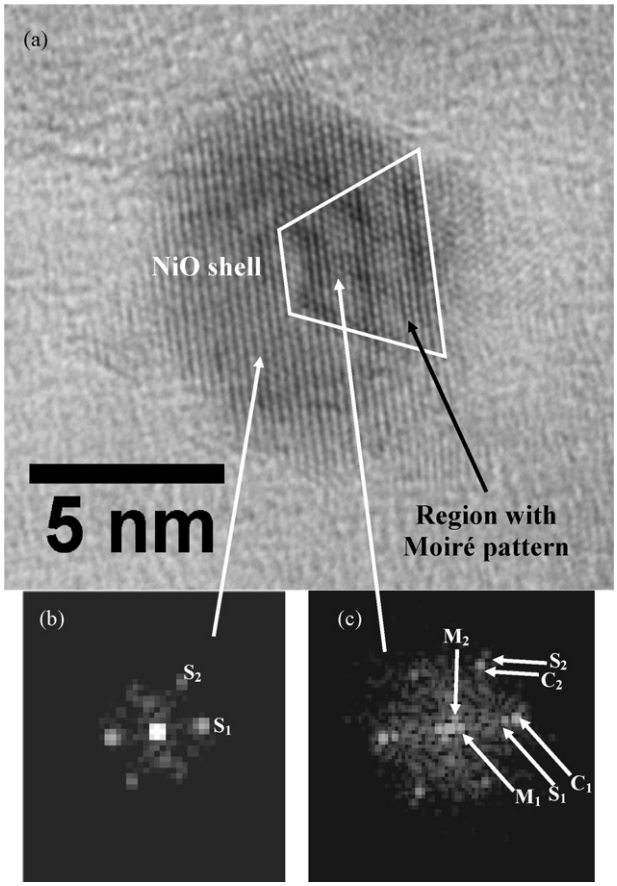

Fig. 8. HRTEM of a large particle presenting an asymmetric core–shell structure (a) and the 2D-FFTs of the shell (b) and the Moiré region (c). S1, S2, C1, C2, M1 and M2 are defined in the text.

Table 2
X-ray photoelectron binding energies (eV) of the nickel–oxygen systems

System	Ni $2p_{3/2}$	O 1s	Reference
Pure Ni	852.7	–	[26,27]
	852.9 + 858.8 (EL)	–	[28]
	852.5	–	[29]
	852.6 (+856.3) + 858.6	–	[25]
	852.6 + ~858	–	This work
NiO	853.8 + EL	529.6	[26]
	854.4	529.5	[27]
	854.5 + 856.3 (MS) + 861.7 (ME)	529.9	[28]
	854	529.6	[29]
	853.7 + 855.8 + 861		[25]
Ni_2O_3	855.8	531.8	[26]
	856		[27]
	855.8 + 861.4 (ME)	531.7	[28]
$Ni(OH)_2$	855.6		[26]
	855.9	531.2	[25]
	855.5 + ~861		[27]
	856.6 + 862.4 (ME)	531.7	[28]
	855.6	531.2	[29]
NiOOH	856.3 + ~861		[25]

The terms EL, MS and ME correspond respectively to energy loss peak, multiplet splitting and charge transfer multielectron excitation (shake up) [28].

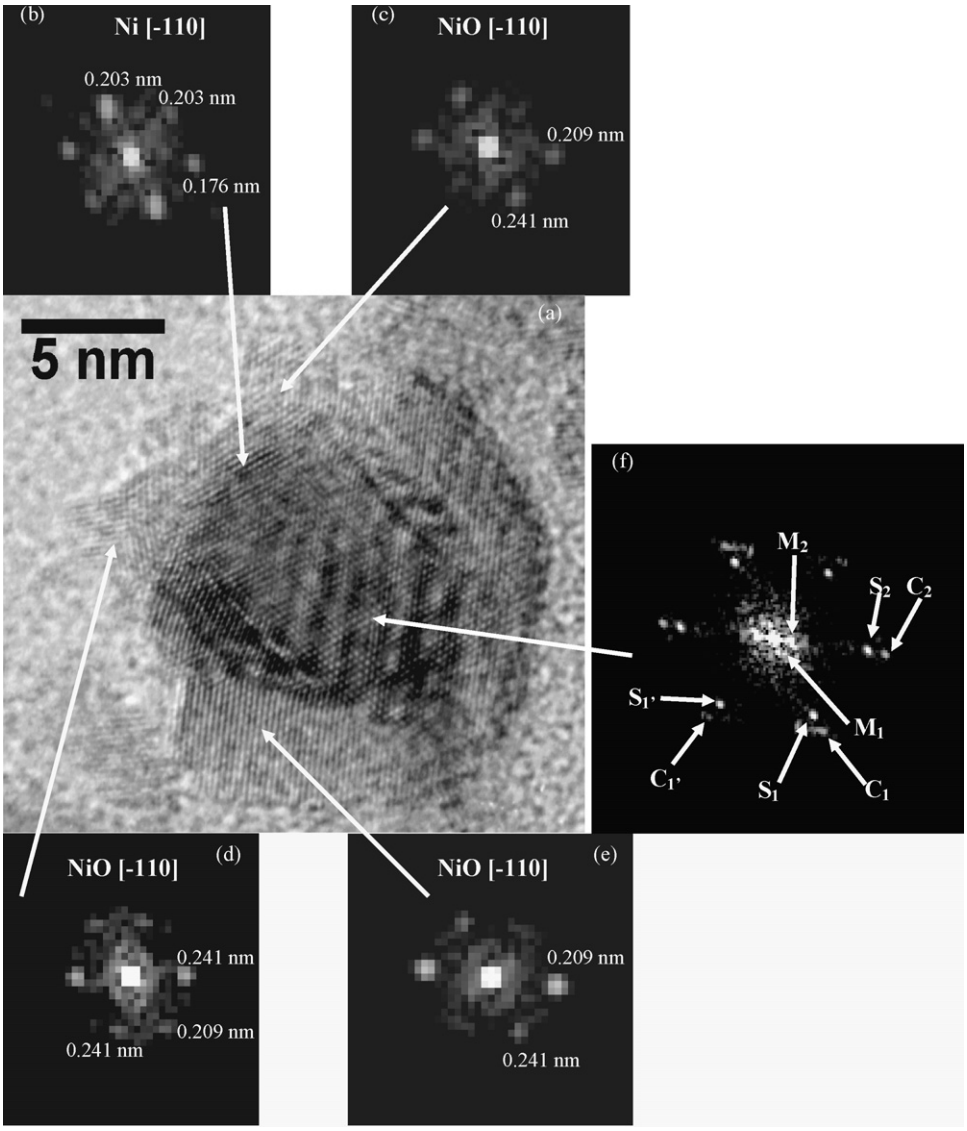

Fig. 9. HRTEM of a core–shell particle with an uncompleted polycrystalline NiO shell (a) with a Ni region on the periphery (b), three different regions of the NiO shell (c–e) and the Moiré region (f) revealed by the 2D-FFTs taken on the respective regions. S1, S1′, S2, C1, C1′ C2, M1 and M2 are defined in the text.

(NiO, Ni_2O_3, $Ni(OH)_2$, NiOOH) [26]. A safe interpretation of the Ni 2p spectra is not trivial. Indeed, the resulting spectra of nickel oxides are envelops of intra-atomic multiplets with many satellite structures [26].

The presence of different states of nickel oxides is confirmed by the spectra in the O 1s region, which show the appearance of (at least) three states of oxygen. Indeed, the spectra can be decomposed in three peaks located at 529.7, 531.5 and 532.8 eV. By taking into account previously published data for XPS spectra of Ni and Ni oxides [27–30] and reported in the Table 2, one can clearly identify the presence of NiO (Ni $2p_{3/2}$ at ~854 eV together with O 1s at 529.7 eV). Nevertheless, the Ni $2p_{3/2}$ spectrum for NiO presents a quite different fine structure with an energy loss peak located near 856 eV less intense than the main peak near 854 eV [26,27,29]. It exists therefore other kinds of Ni oxides. The presence of O 1s peaks located near 531.5 and 532.9 eV, in addition to the peak at 529.7 eV characteristic of NiO, could attest in favour of this statement. With respect to the reference data reported in Table 2, we can propose that the O 1s peak at 531.5 eV is associated to the presence of Ni_2O_3 and/or $Ni(OH)_2$. However, the presence of NiOOH species cannot be ruled out. Attribution of the high energy structure (near 532.8 eV) remains questionable. It has to be noticed that such a peak has been seen for highly oxidised nickel surface.

We can try to get additional information by looking at the LMM Ni Auger spectra (Fig. 12). The maximum located near 846.5 eV is coherent with the presence of metallic Ni both on pure Ni and in the region ‘‘out of the laser impact zone’’; it is at 846.1–846.3 eV for pure Ni [27–29]. The maximum is expected at a lower kinetic energy (KE) for NiO and $Ni(OH)_2$ (respectively at 843.7 and 842.3 eV), but at a higher KE (854.4 eV) for Ni_2O_3 [29]. Therefore, the LMM Auger spectrum measured on the ‘‘laser impact zone’’ let us think that the presence of $Ni(OH)_2$ is more probable than that of Ni_2O_3.

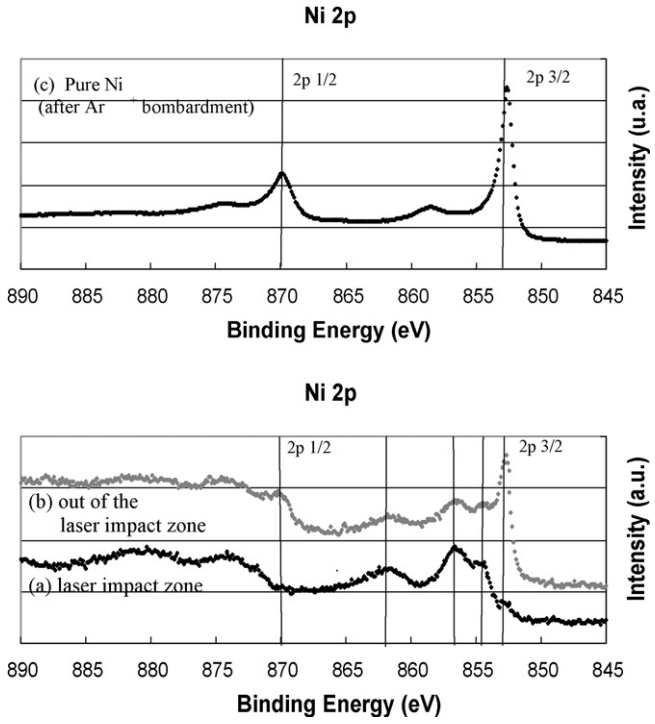

Fig. 10. Ni 2p XPS spectra obtained after impact (10 min) of the Ni target: (a) zone impacted by the laser beam, (b) out of the zone impacted by the laser beam and (c) after argon ion bombardment (clean Ni).

Looking at Fig. 10 it is clear that the ''out of the laser impact zone'' area contains more Ni^0 and less Ni oxides than the ''laser impact zone''. This is confirmed when considering the O/Ni atomic ratio deduced from the O 1s and Ni $2p_{3/2}$ XPS spectra; it is respectively equal to 2.6 and 1.3 for the ''laser impact zone'' and the ''out of the laser impact zone''. The amounts of oxygen seem to be quite high with respect to the stoichiometry of the nickel oxides previously discussed, but the presence of some oxygen pollution at the surface cannot be ruled out in such an analysis process.

In summary, nickel oxides do exist both on the ''laser impact zone'' and on the ''out of the laser impact zone''. Their presence is a priori not obvious on the ''out of the laser impact zone''; but, it is known that besides nanoparticles production surface coating of the areas located out of the impacted zone can exist during laser ablation of solids in liquids [23].

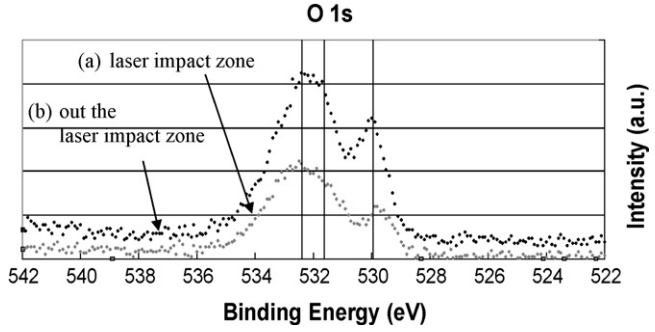

Fig. 11. O 1s XPS spectra obtained after impact (10 min) of the Ni target: (a) zone impacted by the laser beam and (b) out of the zone impacted by the laser beam.

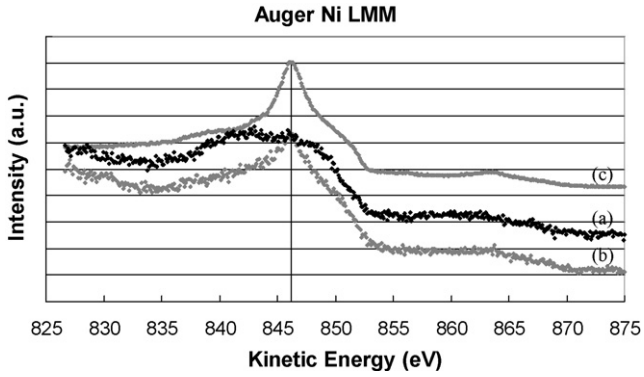

Fig. 12. LMM Ni Auger spectra obtained after impact (10 min) of the Ni target: (a) zone impacted by the laser beam, (b) out of the zone impacted by the laser beam and (c) after argon ion bombardment (clean Ni).

In conclusion, the production of NiO particles in water can be due to the ablation of species containing both Ni and O directly from the oxidised nickel surface impacted by the laser beam. However, the formation of Ni nanoparticles could exist for the early stages of laser ablation, followed by further accretion and total or partial oxidation leading to small single crystal NiO particles and larger core–shell (Ni–NiO) particles.

4. Summary and conclusion

Ablation of Ni targets in water by laser impact (532 nm, 40 mJ/pulse, 10 Hz and 8 ns duration) focused on massive samples (∼2 mm diameter) generates colloids with fine nanoparticles.

The weight loss of the metal target, and therefore the metal released in the solution increases with ablation time, but slower than expected for a process with constant ablation efficiency. This is probably related to the abundance of the nanoparticles in liquid which could interact with the laser beam and thus lower the laser power on the metal sample surface.

Actually, pulsed laser ablation of the nickel target in aqueous solutions produces nanoparticles in the range 3–5.3 nm in diameter, the mean diameter and the size distribution decreasing with increasing the ablation time. This can be explained by a redistribution of the size of the particles through their interaction with the laser beam. The small particles (<8 nm) show a crystalline phase of nickel oxide, but some large particles (>8 nm) show a core–shell contrast with Moiré patterns which is formed by a Ni central core surrounded by a NiO shell.

XPS photoemission measurements evidenced the presence of different nickel oxide species on the crater caused by the laser shots on the nickel target surface that can lead to the formation of NiO nanoparticles.

Acknowledgements

The authors thank Laurence Massin for her expert assistance with the XPS measurements and for continuing discussions on XPS spectra. Rami Mahfouz is grateful to the National Council for Scientific Research (Lebanon) for providing a Ph.D. grant.

References

[1] G. Schmid (Ed.), Cluster and Colloids, VCH, Weinheim, 1994.
[2] M.J. Takagi, J. Phys. Soc. Jpn. 9 (1954) 359.
[3] H. Sakurai, M. Haruta, Appl. Catal. A. Gen. 127 (1995) 93.
[4] N. Ichinose, Y. Ozaki, S. Kashu, Superfine Particle Technology, Springer, London, 1992.
[5] R.D. Sanchez, J. Rivas, C. Vázquez-Vázquez, A. Lopez-Quintela, M.T. Causa, M. Tovar, S. Oseroff, Appl. Phys. Lett. 68 (1996) 134.
[6] J.P. Wilcoxon, J.E. Martin, F. Parsapour, B. Wiedenman, D.F. Kelley, J. Chem. Phys. 108 (1998) 9137.
[7] M. Haruta, S. Tsubota, T. Kobayashi, H. Kageyama, M.J. Genet, B. Delmon, J. Catal. 144 (1993) 175.
[8] C.-B. Hwang, Y.-S. Fu, Y.-L. Lu, S.-W. Jang, T.-T. Chou, C.R. Chris Wang, S.J. Yu, J. Catal. 195 (2000) 336.
[9] S. Kim, B.K. Yoo, K. Chun, W. Kang, J. Choo, M.S. Gong, S.W. Joo, J. Mol. Catal. A: Chem. 226 (2005) 231.
[10] M.F. Becker, J.R. Brock, H. Cai, D.E. Henneke, J.W. Keto, J. Lee, W.T. Nichols, H.D. Glicksman, Nanostructured Materials, vol. 10, no. 5, Elsevier Science Ltd., 1998, pp. 853–863.
[11] S. Link, C. Burda, B. Nikoobakht, M.A. El-Sayed, J. Phys. Chem. B 104 (2000) 6152.
[12] S. Link, M.A. El-Sayed, J. Phys. Chem. B 103 (1999) 4212.
[13] A.V. Smakin, V.V. Voronov, G.A. Shafeev, R. Brayner, F. Bozon-Verduraz, Chem. Phys. Lett. 348 (2001) 182.
[14] I. Lee, S.W. Han, K. Kim, Chem. Commun. (2001) 1782.
[15] N.V. Tarasenko, A.V. Butsen, E.A. Nevar, N.A. Savastenko, Appl. Surf. Sci. 252 (2006) 4439.
[16] M. Kawasaki, N. Nishimura, Appl. Surf. Sci. 253 (2006) 2208.
[17] T. Tsuji, K. Iryo, Y. Nishumura, M. Tsuji, J. Photochem. Photobiol. 145 (2001) 201.
[18] W.T. Nichols, T. Sasaki, N. Koshisaki, J. Appl. Phys. 100 (2006) 114913.
[19] F. Mafuné, J.Y. Kohno, Y. Takeda, T. Kondow, J. Phys. Chem. B 107 (2003) 4218.
[20] C.-B. Hwang, Y.-S. Fu, S.-W. Jang, P.-T. Chou, C.R. Chris Wang, S.J. Yu, J. Catal. 195 (2000) 336.
[21] A. Semerok, C. Chaléard, V. Detalle, J.L. Lacour, P. Mauchien, P. Meynadier, C. Nouvellon, B. Sallé, P. Palianov, M. Perdrix, G. Petite, Appl. Surf. Sci. 138 (1999) 311.
[22] P.V. Kazakevich, A.V. Simakin, G.A. Shafeev, G. Viau, Y. Soumaré, F. Bozon-Verduraz, Appl. Surf. Sci. 253 (2007) 7831.
[23] G.W. Yang, Progr. Mater. Sci. 52 (2007) 648.
[24] P. Hirsh, A. Howie, R. Nicholson, D.W. Pashley, M.J. Whelan, Electron Microscopy of Thin Crystals, second revised edition, Robert E. Krieger Publishing Co., Malabar, FL, USA, 1977.
[25] B. Liu, Z. Hu, Y. Che, Y. Chen, X. Pan, Appl. Phys. Lett. 90 (2007) 044103.
[26] A.P. Grosvenor, M.C. Biesinger, R.St.C. Smart, N.S. McIntyre, Surf. Sci. 600 (2006) 1771.
[27] J.F. Moulder, W.F. Stickle, P.E. Sobol, K.D. Bomben, in: J. Chastain (Ed.), Handbook of X-ray Photoelectron Spectroscopy, Perkin-Elmer Corporation, Physical Electronics Division, 1992.
[28] D. Briggs, M.P. Seah, Practical Surface Analysis, second edition, vol. 1: Auger and X-ray Photoelectron Spectroscopy, John Wiley and Sons, Chichester, 1990.
[29] K.S. Kim, N. Winograd, Surf. Sci. 43 (1974) 625.
[30] N.S. McIntyre, G. Cook, Anal. Chem. 47 (1975) 2208.